NASA Technical Memorandum 82777

Comparison of Two and Three Dimensional Flow Computations with Laser Anemometer Measurements in a Transonic Compressor Rotor

Rodrick V. Chima and Anthony J. Strazisar
Lewis Research Center
Cleveland, Ohio

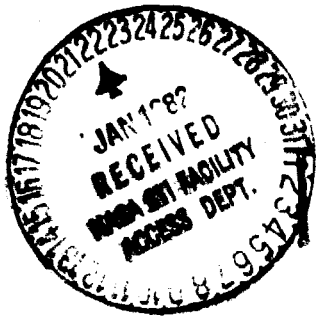

Prepared for the
Twenty-seventh Annual International Gas Turbine Conference
sponsored by the American Society of Mechanical Engineers
London, England, April 18-22, 1982

NASA

COMPARISON OF TWO AND THREE DIMENSIONAL FLOW COMPUTATIONS WITH LASER ANEMOMETER MEASUREMENTS IN A TRANSONIC COMPRESSOR ROTOR

Rodrick V. Chima and Anthony J. Strazisar
NASA Lewis Research Center
Cleveland, Ohio

ABSTRACT

Two and three dimensional inviscid solutions for the flow within a transonic axial compressor rotor at design speed are compared to laser anemometer measurements at maximum flow and near stall operating points. Computational details of the 2-D axisymmetric stream function solution and the 3-D full Euler solution are described. Upstream of the rotor the 2-D and 3-D solutions for radial distribution of relative Mach number and total pressure agree well with the data. Within the bow wave system and the blade row the axisymmetric 2-D solution shows only qualitative agreement with the data. Comparisons are made between relative Mach number contours, shock location, and shock strength as measured and as predicted by the 3-D code. Comparisons at maximum flow show reasonably good agreement at all span-wise locations but also some disagreement due to viscous effects. Comparisons near the tip for the near stall case show excellent agreement. Downstream of the rotor the inviscid computations agree with each other but predict higher pressure ratios than those measured. Euler codes typically require a downstream pressure as input. Since that pressure controls the computed mass flow and shock system, it must be consistent with an inviscid solution. A procedure for using an efficient axisymmetric code to generate downstream pressure input for more costly Euler codes is discussed.

INTRODUCTION

Computational and experimental techniques for the study of flows in turbomachinery are evolving concurrently and are mutually supportive. Experiments provide data for empirical correlations of phenomena that cannot yet be computed such as turbulence. Experimental data may also be used to verify direct computations of flow phenomena. Computational methods can solve for thermodynamic quantities that cannot be measured by optical techniques. Computational methods are also becoming important tools for the development of advanced turbomachine components, and may be used to screen new designs before resorting to more costly experiments.

Advances in both computational and experimental fluid mechanics have been paced largely by advances in electronics, particularly in digital data acquisition and processing. In a 1958 NACA report [1], tip static pressures were measured in a transonic compressor rotor using oscilliscope traces of signals from four pressure transducers embedded in the shroud. Experimentalists now rely on digital data acquisition and reduction systems coupled with traversing pressure and temperature probes for pitchwise averaged flow measurements upstream and downstream of rotors [2]. Two-dimensional through-flow analysis codes like [3] are the computational counterparts of these probe measurements. Current data processing equipment coupled with electro-optical sensors allows the experimentalist to make detailed maps of the core flow in rotating compressors, [4 and 5]. Three-dimensional analysis codes like [6] are the computational counterparts of current laser anemometer measurements. Experimentalists are just beginning to take measurements inside the viscous layers on blade rows. Similarly, computational methods are now being developed to analyze two-dimensional viscous flows in cascades [7]. It seems likely that the latest generation of supercomputers and continuing advances in instrumentation will allow both computational and experimental work to progress even further, and that the resulting gains in understanding will lead to improvements in turbomachinery performance.

It is important to note that the early experimental and analytical work is still extremely important. In fact this paper relies heavily on all of references [1 through 6] mentioned above. Before going into the details of the present work, it may be of interest to review current literature comparing optical measurements and computations of flows in turbomachinery.

Optical techniques that have been used for flow measurements in turbomachinery include holographic interferometry [8], the gas fluorescence technique [9], the laser-two-focus technique (L2F, also called laser transit anemometry or LTA) [10 and 11], and laser anemometry (LA, also called laser Doppler

velocimetry or LDV) [4 and 5]. The LA technique reported in [5] was used in the present work.

Computational methods used to calculate flows in turbomachinery include 2-D through-flow codes [3, 12, and 16], 2-D steady blade-to-blade codes [13 and 14], 2-D unsteady blade-to-blade codes [15 and 16], quasi-3-D codes [13 and 16], and fully 3-D codes [6 and 17]. The 2-D through-flow code in [3] and the 3-D code in [6] were used in the present work.

The following references compare optical measurements and computations of flows in turbomachinery. Several references have compared computations to L2F measurements in a transonic rotor designed and tested at DFVLR. Reference [12] compares these measurements with through-flow calculations at a full speed operating point. Reference [13] compares them with a quasi-3-D solution at a subsonic part speed operating point, and reference [16] compares them with a quasi-3-D time-marching solution at three transonic operating conditions. A fully 3-D solution for transonic flow in the DFVLR rotor is presented in [17]. Comparisons between LTA measurements and steady blade-to-blade solutions of the flow in a low speed four stage GE research rotor are given in [14]. Reference [15] gives an early comparison between LA measurements and a steady blade-to-blade solution in a GE transonic fan. Reference [18] compares gas fluorescence measurements with a 3-D time-marching solution for a NASA low aspect ratio transonic fan.

The present work compares conventional probe measurements, LA measurements, 2-D through-flow computations, and 3-D Euler computations of transonic flows in a NASA-designed core compressor inlet rotor. These comparisons are made at design speed at two operating points, a maximum flow point and a near stall point. Comparisons between measured and computed data are made for total pressures and relative Mach numbers along grid lines, for nominal relative Mach numbers on the blade surfaces, for contour plots of relative Mach numbers and flow angles on grid planes, for shock locations and strengths, and for mass flows and total pressure ratios. These comparisons are intended to demonstrate the capabilities of the analysis codes for predicting two widely different flow conditions in an actual machine.

In reference (8) similar comparisons were made between LA data and a 3-D Euler solution of the maximum flow operating point for this rotor. Good comparisons were found near the tip, but the computed shock structures at midspan and near the hub were incorrect. Bow waves were poorly resolved. Several improvements over reference (8) have been made in the present work. First, bow wave resolution has been improved by increasing the grid size and by clustering the grid around the leading edge. Second, shock structures have been improved by replacing measured exit hub static pressure input to the code with values calculated using a 2-D through-flow code. The procedure used to calculate appropriate boundary values is described in detail later. Third, the near stall results presented here may be of more interest to designers since these results are more representative of a typical compressor design point.

EXPERIMENTAL APPARATUS

Compressor Rotor

Rotor 33 was designed at NASA Lewis Research Center as an inlet rotor for a core compressor. The flowpath consists of a constant radius hub and a converging tip. At the inlet the tip radius is 254 mm (10 in) and the hub/tip radius ratio is 0.7 . The rotor has 52 blades with a tip chord of 44.5 mm (1.75 in) and a tip solidity of 1.48 . At the design speed of 16,100 rpm the tip speed is 426 m/sec (1398 ft/sec.)

The rotor was tested without inlet guide vanes or stators, thereby eliminating any circumferential variations that would be introduced by stationary blade rows. Radial surveys of total pressure, total temperature, flow angle, and static pressure were taken upstream and downstream of the blade row using conventional probes [2]. The upstream and downstream measurement stations, designated stations one and two, were located one chord upstream and one-half chord downstream of the rotor respectively.

Data for this paper were taken at design speed at two throttle settings, a wide open maximum flow setting and a partially closed near stall setting. At maximum flow the rotor pressure ratio was 1.49 and the mass flow was 208 kg/sec/m^2 (42.40 lbm/sec/ft^2). Mass flows were measured using a calibrated orifice located far upstream. Inlet relative Mach numbers at maximum flow ranged from 1.14 near the hub to 1.35 near the tip. Near stall the rotor pressure ratio was 1.66 and the mass flow was 191 kg/sec/m^2 (39.12 lbm/sec/ft^2). Inlet relative Mach numbers near stall ranged from 1.05 near the hub to 1.32 near the tip.

Laser Anemometer

The fringe type laser anemometer (LA) [4] is a single channel dual beam system with on-axis backscatter light collection. A dedicated minicomputer, a disk storage system, and a CRT display were used for real time data acquisition and processing. The minicomputer was also

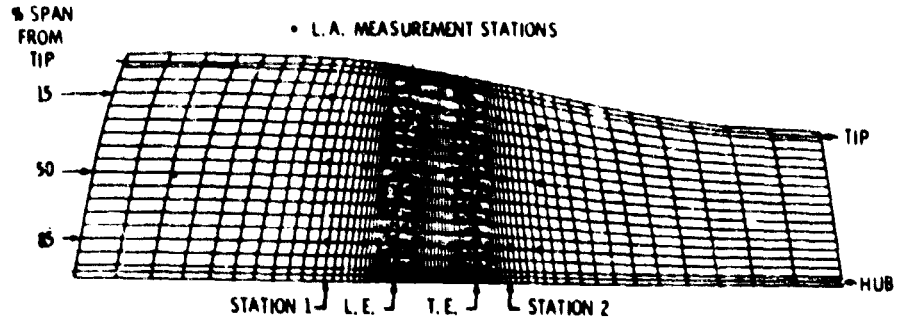

Figure 1. - Meridional view of the computational grid showing L.A. measurement stations and conventional probe measurement stations.

connected to a large central computer for additional data processing and graphical output.

A window fabricated from commercial window glass provided optical access to the compressor. The window conformed to the outer endwall contour and measured 102 mm axially by 51 mm in circumference (11 degrees arc) by 3 mm thick.

Seed particles consisted of spray-atomized rhodamine 6G dye dissolved in a solution of benzyl alcohol and ethelyene glycol. The particles were injected into the flow 460 mm upstream of the rotor. Exposed to laser light the seed particles fluoresce orange. An orange-pass optical filter placed in front of the photomultiplier selectively removed unwanted green laser light reflected from the hub and blades. The seed particle diameter was determined by equating the particle velocity lag measured downstream of the rotor passage shock to that predicted by a one-dimensional Stokes drag model and solving for the unknown particle diameter. The particle diameter found by this procedure was 1.2-1.5 micrometers [5].

An efficient data acquisition system made it possible to map the blade-to-blade distribution of a velocity component at a given axial and radial position very quickly. Whenever a seed particle crossed the probe volume the particle velocity and the rotor shaft angular position were recorded as a data pair. Approximately 30 measurements were made at each of 1000 different shaft positions distributed as 50 positions per blade passage over 20 consecutive blade passages. The 30 velocities and flow angles at each shaft position were averaged to give time-averaged velocity distributions over 20 consecutive passages. The time-averaged distributions were analyzed to detect variations between individual passages [5]. The 20 time-averaged velocity distributions were spatially-averaged to yield the velocity distribution across an average passage. A typical run consisting of 30,000 measurements at a single axial and radial position took between 15 and 45 seconds.

Errors in the LA measurements arise from a number of sources. The sources of error and the corresponding error magnitudes have been discussed in detail in [5] and will only be summarized here. Passage-to-passage velocity variations were on the order of five percent for most runs. Spatial averaging of data obtained across 20 blade passages improves the statistical accuracy of the data. Compressor speed drift during a run was on the order of 0.3 percent and the repeatability of a given run was one percent. The error in velocity and flow angle measurements which encompassed 95 percent of the data was generally five percent or less except in regions immediately downstream of shocks where seed particle velocity lag was the dominant error. The observed lag distance required for the seed particles to achieve 95 percent of the post-shock gas velocity was found to be 13 percent of chord for the maximum flow case at 15 percent span from the tip. The LA data has not been corrected for particle lag since velocity variations due to particle lag cannot in general be distinguished from those occurring due to the compression process.

Figure 1 shows the LA measurement stations and probe survey stations superimposed on the finite difference grid used with the 3-D code. Typically 22 measurement stations lie along each of three design streamlines located at 15, 50, and 85 percent span from the tip with 12 of the axial stations within the blade row. The three radial locations lie within one percent span of the grid lines shown. At the near stall operating point LA measurements were only taken at 15 percent span from the tip.

COMPUTATIONAL METHODS

Two-Dimensional Through-Flow Code MERIDL

The through-flow analysis code used in the present work is the MERIDL code [3]. The code solves an axisymmetric inviscid momentum equation for a stream function along a midchannel hub-shroud stream surface. The stream function is defined to satisfy continuity identically, and is differentiated numerically to find individual velocity components. Thermodynamic quantities are found from isentropic relations. Rotation, passage convergence, blade row turning, and blockage are all accounted for in the formulation. A successive over relaxation finite difference technique is used to solve the nonlinear stream function equation. An orthogonal finite difference grid with 10 points radially and 40 points axially (10 points upstream and downstream, 20 within the blade row) was used for the present calculations. While the grid is not shown here, it had the same extent as the 3-D grid shown in Figure 1. Input to MERIDL consists of blade, hub, and tip geometry, mass flow, upstream total conditions, up and downstream whirl (rV_θ) distributions, and axial and radial distributions of total pressure loss. Upstream total conditions were input as constants radially, and the upstream whirl was set to zero. The exit whirl was taken as a smooth curve fit through the measured probe data, excluding points obviously in the endwall boundary layers.

Three-Dimensional Euler Code BLADE3D

The 3-D analysis code used in the present work is the BLADE3D code described in [6]. Only a brief description is given here. The equations solved are the inviscid unsteady Euler equations written in cylindrical coordinates and in non-conservative form. The equations include the continuity equation, the axial, radial, and circumferential momentum equations, and the energy equation, which are solved for the density, three velocity components, and total energy. Pressure is found from the ideal gas law. Blade row rotation is specified.

MacCormack's explicit time-marching finite difference method in split operator form [19] is used to advance the unsteady solution in time from an initial guess to a converged steady solution. The method is second order accurate and conditionally stable. Shocks are captured automatically and smeared over several grid points. Artificial viscosity terms are added to improve stability near shocks, but they also increase shock smearing.

Algebraic mappings are used to transform the complex flowpath geometry into a rectangular computational domain. The computational mesh had 100 axial points (32 points upstream and downstream, 34 within the blade,) 17 circumferential points, and 18 radial points. Axially the grid points were clustered around the leading and trailing edges to impove resolution of bow and shock waves. Points were stretched upstream and downstream to allow imposition of axisymmetric far field conditions. Radially and circumferentially the points had constant spacing. A sheared blade-to-blade grid was used. Figure 1 shows a meridional view of the grid.

At the inlet grid plane the flow is assumed to be axisymmetric and is matched to desired conditions at upstream infinity where total conditions are specified, the radial velocity is zero, and the whirl is specified (here also zero.) The non-reflective inlet boundary condition is based on the one-dimensional method of characteristics. The desired axial velocity and static temperature at upstream infinity are combined to form a single variable, the value of the downstream-running characteristic. This value may be computed from the desired mass flow or upstream Mach number using isentropic relations, or from MERIDL output. Although the BLADE3D solution is sensitive to the input characteristic value, all methods of computing that value give consistent results. The intersection of the specified downstream-running characteristic and the computed upstream-running characteristic at the inlet determine the inlet static temperature and axial velocity. Thus the mass flow is computed as part of the solution and may not necessarily match the measured value.

At the exit grid plane the flow is also assumed to be axisymmetric and the radial velocity is set to zero. The exit circumferential velocity, density, and downstream-running characteristic are extrapolated from within the flow field. Only one boundary value is specified, the hub static pressure at the exit of the computational domain. A radial equilibrium equation is integrated from hub to tip at the exit to determine the radial pressure distribution, which supplies the final unknown at the exit.

Other boundary conditions used in the BLADE3D code include periodicity up and downstream of the blade row, tangency on the hub, shroud, and blade surfaces, and a Kutta condition specifying constant static pressure across the blade trailing edge.

Exit Pressure Specification

Euler codes typically require that the exit static pressure be specified as a boundary condition when the exit flow is subsonic. This input variable controls the computed mass flow and shock

structure, and must be specified correctly to produce reasonable solutions. Experience with the BLADE3D code has shown that use of measured values of exit hub static pressures tends to produce solutions with higher mass flows and stronger shocks than those measured. This appears to be due to the neglect of viscous blockage and losses. Without these viscous effects, the BLADE3D code predicts higher mass flows for a given static pressure rise, or conversely, predicts a higher static pressure rise for a given mass flow than would be found in a viscous flow. Hence, to compute a case with a given mass flow a designer must input an exit static pressure somewhat higher than measured. That exit pressure can be varied iteratively to match the desired mass flow, but computational times may become prohibitive.

Since the desired mass flow is an input variable for the MERIDL code and static pressures are included in the output, and since a MERIDL solution can be run in about a minute of computer time, the MERIDL code can be used effectively to estimate exit hub static pressures for the BLADE3D code.

Measured values of mass flow, upstream total conditions, and inlet and exit whirl are input to MERIDL as described earlier. One piece of input remains to be described, the axial and radial distributions of total pressure loss. Since MERIDL is incapable of predicting either shock or viscous losses, the amount of loss specified can make a MERIDL solution compare well with either measured data or a BLADE3D solution. For best comparison with measured data, measured losses must be input. But for best comparison with a BLADE3D solution, only shock losses must be input.

The axial distribution of the loss has little or no effect on the exit static pressure, so losses may be distributed evenly within the blade row. Radial distributions of shock losses in rotor 33 were calculated as part of the probe data reduction using the Miller-Hartmann model described in [1]. The model estimates shock losses to be those occurring across a single normal shock standing near the passage entrance. The Mach number ahead of the shock is taken as the average of the inlet relative Mach number and a somewhat higher value on the suction surface near the shock intersection.

At the near stall operating point rotor 33 has a single shock system like the one in the Miller-Hartmann model, but at the maximum flow point it has a two shock system that is not modelled correctly. Overall the BLADE3D near stall solution compares better with the LA data than the maximum flow solution does. Much of this is attributed to the better fit of the near stall shock structure to the Miller-Hartmann model.

	$\dot{m}(kg/sec/m^2)$	$\dot{m}(lbm/sec/ft^2)$	tot.pres.ratio
LA	208.	42.6	1.49
BLADE3D	218.	44.6	1.71
MERIDL	208.*	42.6 *	1.64

Table 1. Comparison of measured and computed mass flows and total pressure ratios, maximum flow point.

***Mass flow is set explicitly as an input to MERIDL.**

Computational Details

Initial conditions for the maximum flow case assumed constant upstream velocity based on a specified inlet Mach number, velocity variations within the blade row based on blade turning, and constant velocity downstream. Solutions were run on an IBM 3030 AP computer. The time step used ranged from 75 to 90 percent of the stability limit. Convergence to a steady state was determined by monitoring the trailing edge pressure distribution which reflects the Kutta condition and the blade loading. Trailing edge pressures were converged to the fourth significant figure.

The maximum flow case took approximately 12 CPU hours (4500 time steps) to converge. The near stall case was calculated as the time-accurate response of the maximum flow case to a 9.6 percent increase in exit hub static pressure and a change in inlet conditions which resulted in an inlet Mach number drop of 0.06. This case took nearly twice as long to converge as the maximum flow case did because of the additional time necessary for the downstream pressure rise to travel upstream against a high subsonic flow. Starting from the nearly constant initial conditions described earlier, the near stall case converges about as fast as the maximum flow case. Thus, when only a steady solution is desired, it is often computationally more efficient to start with a simple initial guess than with a converged solution for a different flow.

The computer times quoted above are large. It should be noted that they were accumulated over many runs by restarting the code. Computer times can be reduced substantially by reducing grid size and grid clustering.

RESULTS AND DISCUSSION

Maximum Flow Operating Point

Since mass flow is computed by BLADE3D and pressure ratio is computed by both BLADE3D and MERIDL, these global parameters are of particular interest. Table 1 shows that the mass flow

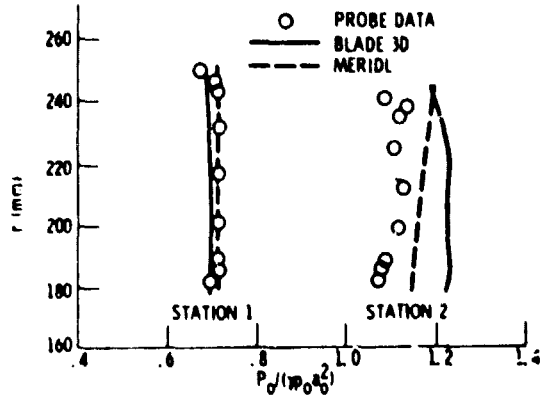

Figure 2. - Radial distribution of circumferentially averaged total pressure, maximum flow point.

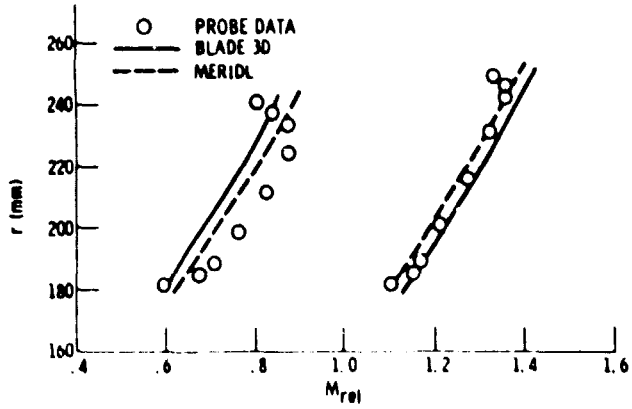

Figure 3. - Radial distribution of circumferentially averaged relative Mach number, maximum flow point.

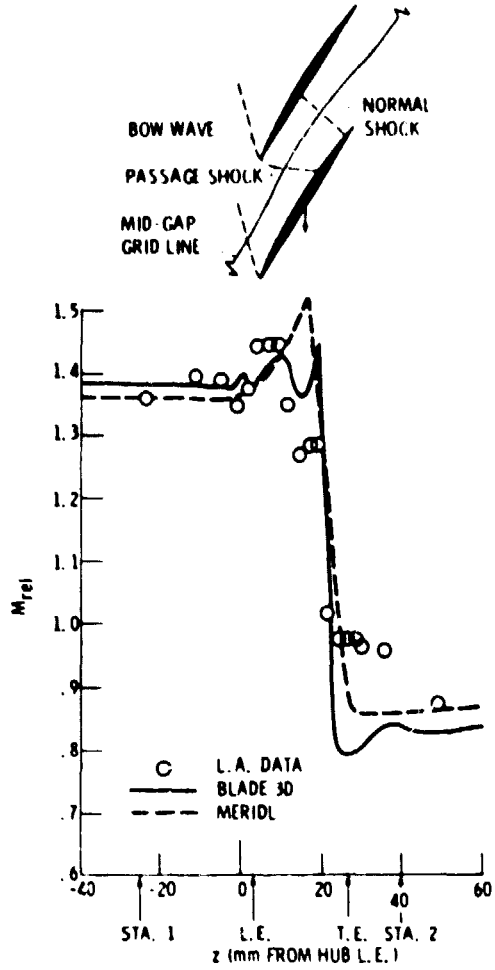

Figure 4. - Axial distribution of relative Mach number, 15 percent span from the tip, mid-gap, maximum flow point.

calculated by BLADE3D is 4.8 percent higher than the measured orifice value. This is a substantial error at this operating point. Nevertheless, other aspects of the BLADE3D solution agree reasonably well with the LA data. Total pressure ratios calculated by both codes are high; BLADE3D is 14.8 percent high and MERIDL is 10.0 percent high. Differences between the BLADE3D and MERIDL solutions are attributed to differences in shock losses calculated by BLADE3D and by the Miller-Hartmann model.

Radial distributions of circumferentially-averaged total pressure and relative Mach number are compared to probe measurements upstream and downstream of the rotor in Figures 2 and 3. Axial locations labeled station 1 and station 2 are shown in Figure 1. Upstream (station 1) the calculations and measurements are in good agreement except for the error due to the high BLADE3D mass flow. Downstream (station 2) the high total pressures calculated inviscidly are evident. Endwall boundary layer effects that cannot be predicted inviscidly are evident in the probe measurements, especially at the tip of station 2.

Axial distributions of relative Mach number at 15 percent span from the tip are compared in Figure 4 . The MERIDL calculations are of course axisymmetric. The BLADE3D and LA results are shown along a mid-gap line. The MERIDL results show little upstream influence of the blades, while the BLADE3D and LA results show relative Mach number fluctuations due to a bow wave system. The computed bow wave is weaker than that measured. Within the blade row the measured and BLADE3D computed flows accelerate slightly, decelerate across an oblique passage shock, and finally decelerate sharply across a normal shock near the trailing edge.The calculated normal shock is stronger than the measured shock, possibly due to the error in the computed mass flow or to the neglect of viscous blockage. Discrepancies between the shock jumps shown and the normal shock tables are due to the inclination of the rear shock relative to the line along which the results are shown. The MERIDL

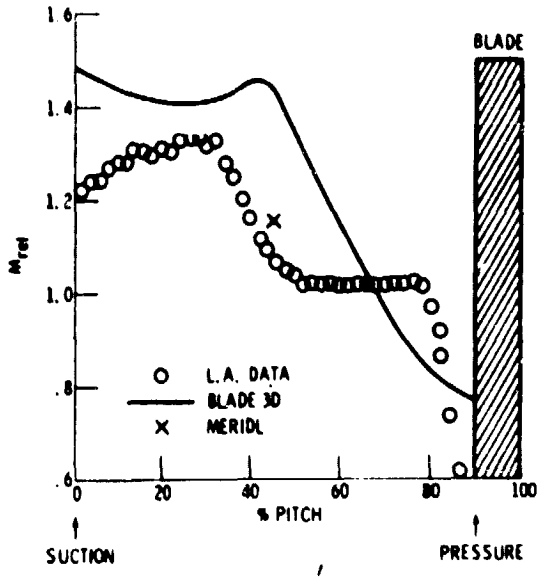

Figure 5. - Circumferential distribution of relative Mach number, 15 percent span from the tip, 78 percent chord (through the rear shock), maximum flow point.

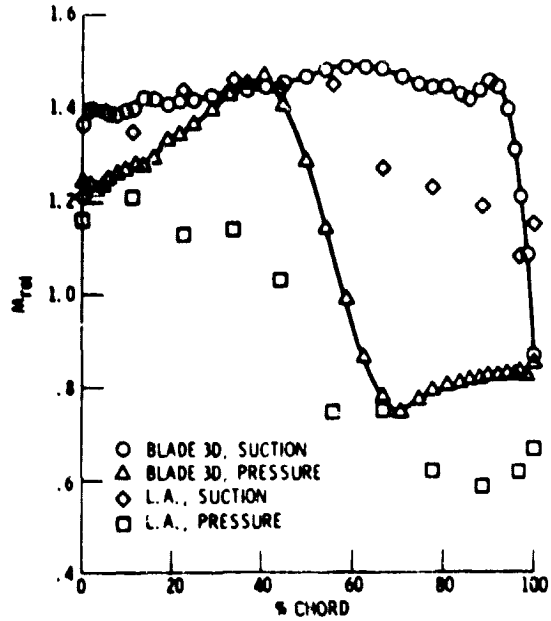

Figure 6. - Axial distribution of relative Mach number on the blade surfaces, 15 percent span from the tip, maximum flow point.

results show surprising agreement inside the blade row, but the agreement is coincidental. The initial acceleration in the MERIDL results is due to blade blockage. The rapid deceleration that appears to be a shock is due to rapid turning of the flow to match the specified downstream whirl. Downstream of the blade row both computed flows reaccelerate slightly due to tip convergence.

Circumferential distributions of relative Mach number at 15 percent span from the tip and at 78 percent chord (through the rear shock) are shown in Figure 5. The abscissa of the plot showing percent gap is measured from the suction surface of a leading blade to the suction surface of the following blade. At this axial location the flow near the suction surface (left) is upstream of the rear shock but the flow near the pressure surface (right) has passed through the shock. It is possible that the measured drop off in Mach number near the pressure surface is caused by shock-boundary layer interaction. The shock location is clearly defined in both the LA measurements and the BLADE3D calculations as an abrupt drop in Mach number near mid-gap. Shock smearing evident in the LA measurements is due to seed particle lag; and shock smearing in the BLADE3D calculations is due to artificial viscosity. Blade boundary layer effects may be evident in the measurements. MERIDL results look reasonable as an axisymmetric average. MERIDL results are omitted from the remaining maximum flow results.

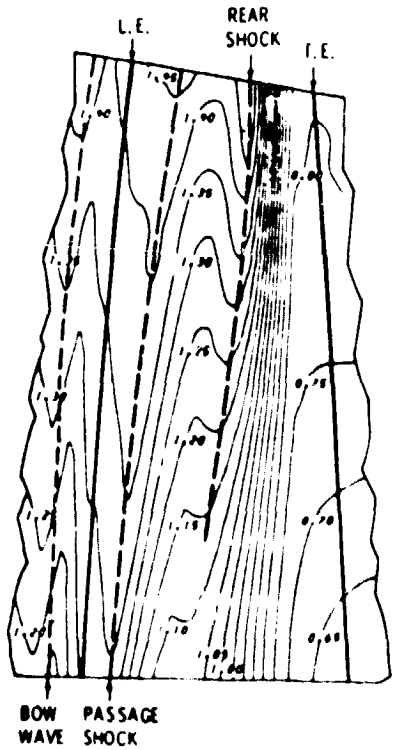

Figure 7. - Computed relative Mach number contours on a mean flow surface at mid-channel, maximum flow point.

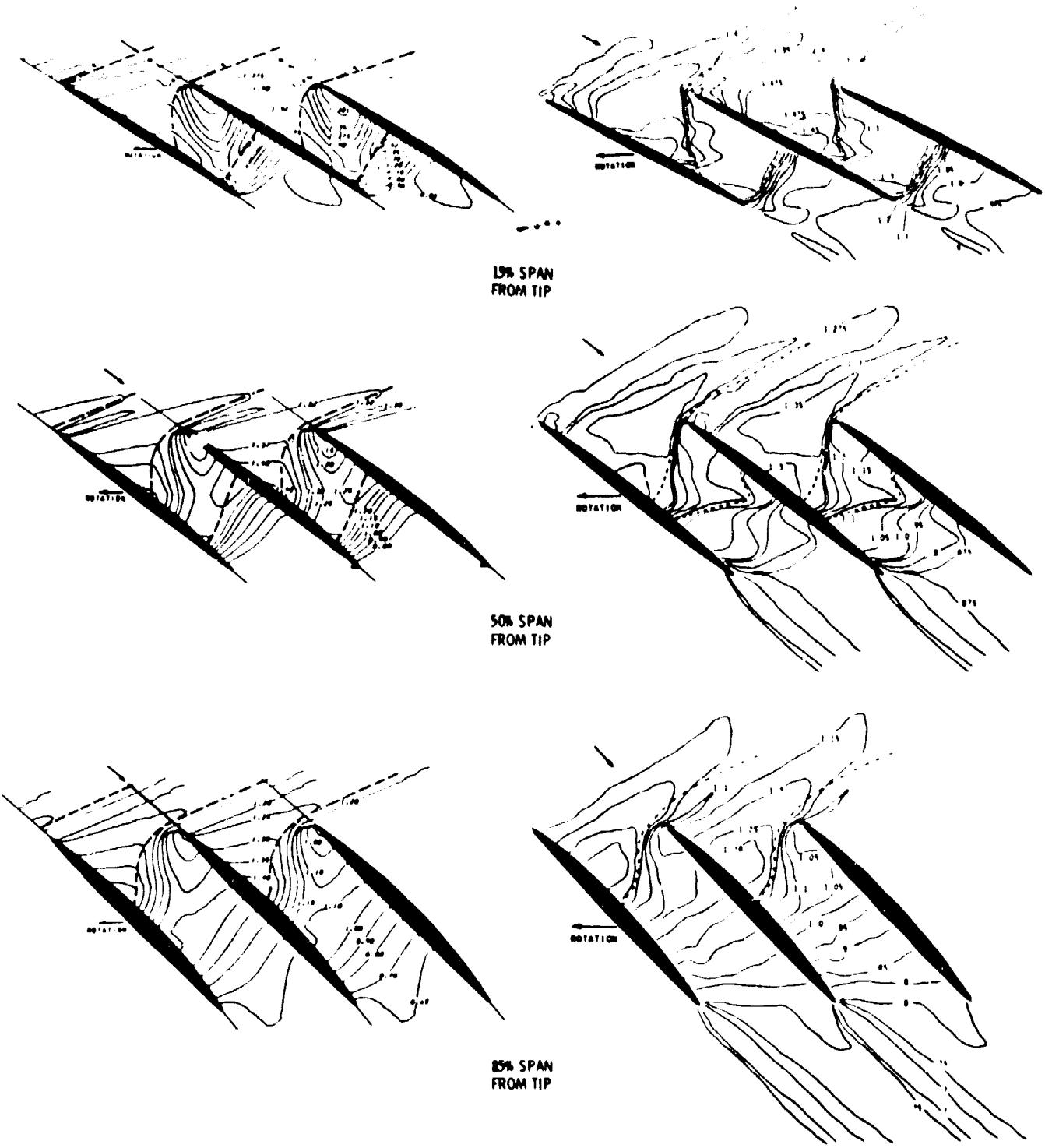

Figure 8 - Blade to blade contours of relative Mach number, maximum flow point

% SPAN FROM TIP	LA				BLADE3D			
	Mrel	βrel	α	ω_s	Mrel	βrel	α	ω_s
15	1.28	52.0	10.	.0037	1.323	50.5	14.	.0161
50	1.37	56.8	5.	.0118	1.387	56.0	7.	.0162
85	1.45	61.6	0.	.0235	1.426	60.9	2.	.0229

Table 2. Comparison of measured and calculated shock loss parameters, rear shock, mid-gap, maximum flow point.

Blade surface relative Mach number distributions along the design streamline at 15 percent span from the tip are shown in Figure 6. LA measurements of surface relative Mach number were taken from plots like Figure 5 as the first circumferential point for which a statistically significant number of measurements was taken (at least 20 measurements.) At a tip chord Reynolds number of about $6*10^5$, an unseparated turbulent blade boundary layer thickness would be of the order of the measurement point spacing; so it is felt that the first statistically significant point should be near the edge of the core flow. Nevertheless, viscous effects may be present in the data. The calculations and measurements show only a qualitative agreement in shock location and the rearward blade loading.

Figure 7 shows contours of computed relative Mach number on a mean flow surface at mid-channel, and is included to show the three-dimensional nature of the solution. Most of the upstream and downstream regions have been omitted. Dashed lines indicate shocks. The rear passage shock is slightly curved from hub to tip. Near the hub it is difficult to distinguish whether there is a rear shock or just a diffuse compression.

Computed and measured blade-to blade relative Mach number contours are compared side by side at the three span-wise locations in Figure 8. Shocks are shown by dashed lines. Computed shock locations were determined from axial plots of relative Mach number like Figure 4 as grid points with maximum Mach numbers before rapid drops. These grid points were located on the blade-to blade plots and fit with a smooth curve. Experimental shock locations were determined similarly except that circumferential plots like Figure 5 were used. At 85 percent span from the tip the computations and measurements are in excellent agreement. Both show a bow wave with an exit Mach number of 1.2 . The calculations show a stronger suction surface acceleration than the data. Both also show a forward passage shock with similar exit Mach numbers and small sonic regions on the pressure surface near the leading edge. Finally both show a diffuse compression to subsonic with no obvious rear shock. The calculated flow exits at a considerably lower Mach number than the measured flow. At midspan the comparison is similar except that here both show a definite rear shock. The measured rear shock is forward in the passage relative to the calculated shock, and may even be a reflection of the front shock. At 15 percent span from the tip the LA measurements show a stronger bow wave and passage shock than the BLADE3D solution . The calculations and measurements both show very strong rear shocks attached to the trailing edge. These results show improved bow wave resolution and rear shock location over the results in reference [8] due to grid refinement and adjustment of the exit hub static pressure.

Shock angles and total pressure loss coefficients for the forward passage shock at the three span-wise locations and at mid-gap are tabulated in Table 2. The shock inclination angle, α, is measured from the axial direction. The shock loss coefficient is defined in [1] as:

$$\omega_s = (1-P_2/P_1)/(1-p_1/P_1)$$

where upper and lower case letter p refer to total and static pressure respectively. The total pressure ratio P_2/P_1 is obtained from the normal shock relations using the component of relative Mach number ahead of and normal to the shock. There is some disagreement between the LA and BLADE3D shock loss coefficients, especially at the hub. Part of the disagreement is due to small discrepancies ahead of the shock; part is due to shock inclination in the meridional plane; but most is due to difficulties in determining the shock angle from shock locations found as described earlier.

	$\dot{a}(kg/sec/m^2)$	$\dot{a}(lb_m/sec/ft^2)$	tot.pres.ratio
LA	191.	39.1	1.66
BLADE3D	188.	38.5	1.866
MERIDL	191. *	39.1*	1.864

Table 3. Comparison of measured and calculated mass flows and total pressure ratios, near stall point.

*Mass flow is set explicitly as an input to MERIDL.

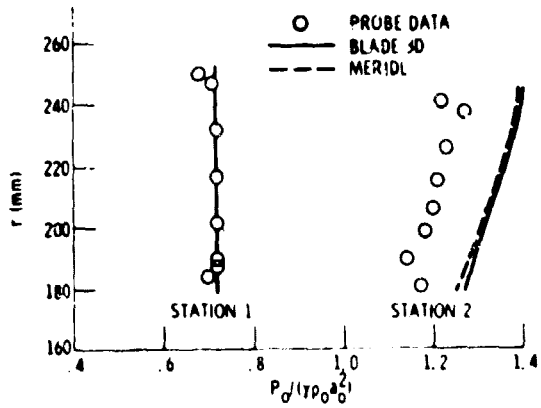

Figure 9 - Radial distribution of circumferentially averaged total pressure, near stall point.

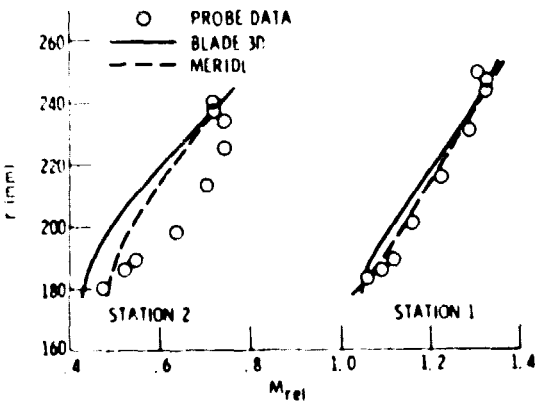

Figure 10 - Radial distribution of circumferentially averaged relative Mach number, near stall point.

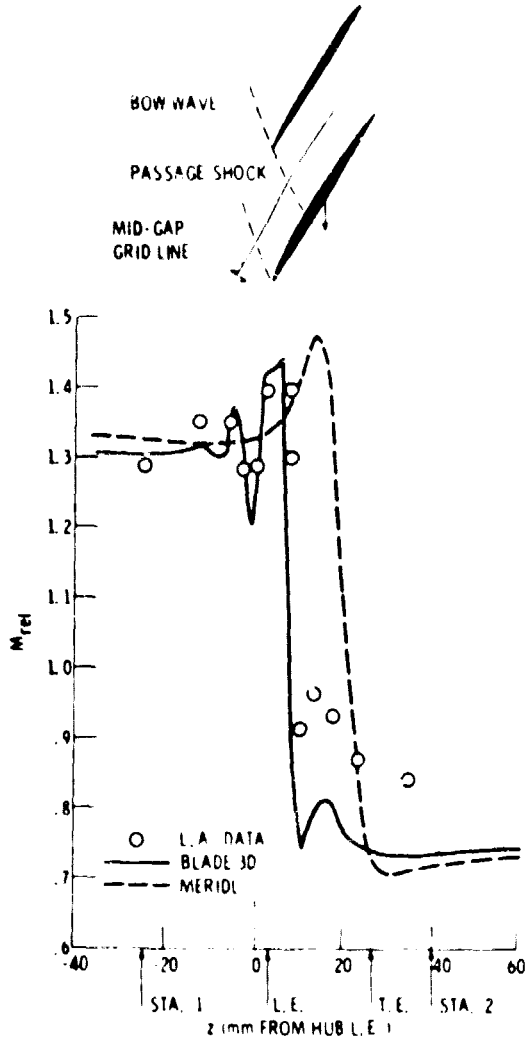

Figure 11. - Axial distribution of relative Mach number, 15 percent span from the tip, mid-gap, near stall point.

Near Stall Operating Point

Mass flow and total pressure ratio for the near stall case are compared in Table 3. The BLADE3D mass flow is 1.5 percent low, and the BLADE3D and MERIDL total pressure ratios are both 12.4 percent high, probably due to neglect of viscous losses and blockage.

Radial distributions of circumferentially-averaged total pressure and relative Mach number shown in Figures 9 and 10 are similar to the maximum flow case except that here the BLADE3D and MERIDL results are in better agreement.

Axial distributions of relative Mach number at 15 percent span from the tip are shown in Figure 11. The BLADE3D Mach numbers show good agreement with the LA measurements in the strong bow wave system and in the location of the passage shock. The passage shock jump is over predicted, again possibly due to the neglect of viscous blockage. The MERIDL results behave as before, showing an initial acceleration due to blockage followed by a rapid compression due to turning. MERIDL cannot capture the upstream wave system or the passage shock, yet the MERIDL results agree fairly well outside the blade row.

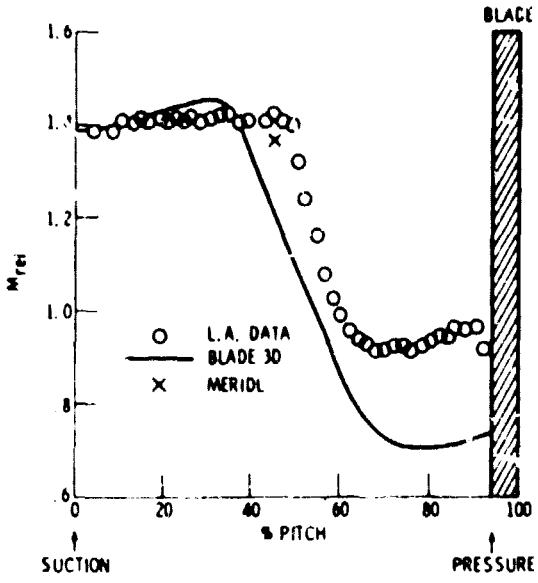

Figure 12. - Circumferential distribution of relative Mach number, 15 percent span from the tip, 23 percent chord (through the passage shock), near stall point.

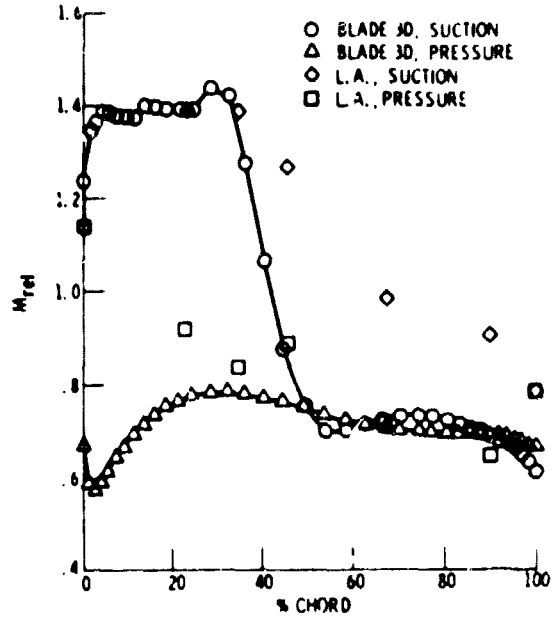

Figure 13. - Axial distribution of relative Mach number on the blade surfaces, 15 percent span from the tip, near stall point.

Circumferential distributions of relative Mach number at 15 percent span from the tip and at 23 percent chord (through the passage shock) are shown in Figure 12. At this axial location the flow near the suction surface (left) is upstream of the passage shock but the flow near the pressure surface (right) has passed through the shock. The Mach number distributions show slight discrepancies in shock location and strength. MERIDL results agree with flow conditions on the upstream side of the shock. MERIDL results are omitted from the remaining near stall results.

Figure 13 compares computed and measured blade surface relative Mach numbers at 15 percent span from the tip. Suction surface shock locations agree to within the measurement spacing. The computed near stall blade loading is dramatically shifted to the front of the blade compared to the maximum flow solution in Figure 6.

Computed relative Mach number contours on a mid-channel mean-flow surface in Figure 14 show a complete change in shock structure from the maximum flow solution in Figure 7. In the near stall solution the bow wave and passage shock are stronger and straighter than in the maximum flow solution. The rear passage shock has been eliminated.

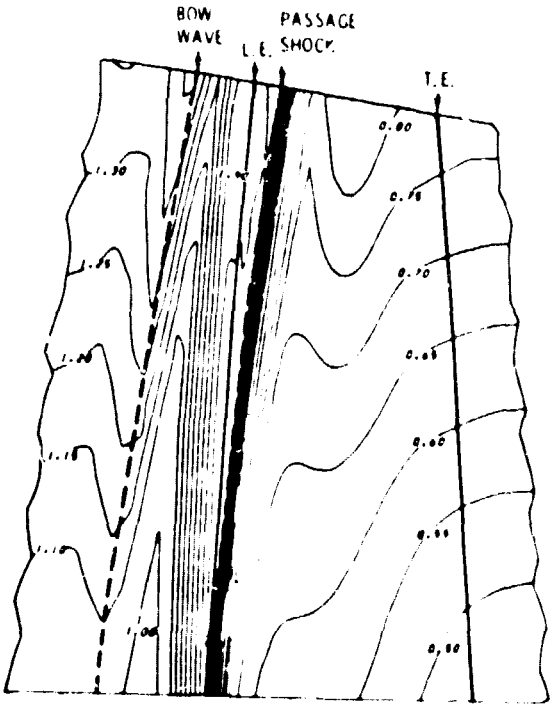

Figure 14. - Computed relative Mach number contours on a mean-flow stream surface at mid-channel, near stall point.

L.A. DATA, - - - - - SHOCK

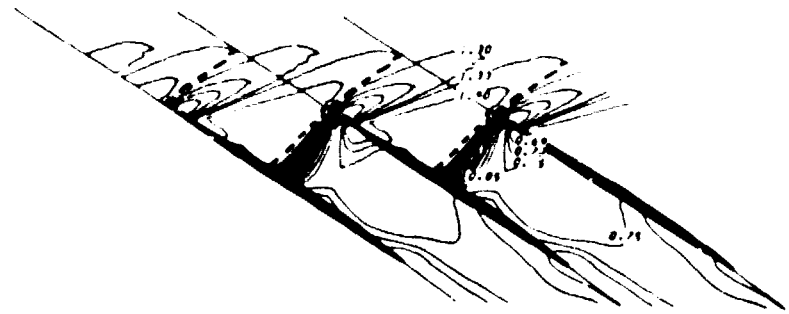

BLADE 3D CALCULATIONS, - - - - - SHOCK

Figure 15. - Blade to blade contours of relative Mach number, 15 percent span from the tip, near stall point.

L.A. DATA, - - - - - SHOCK

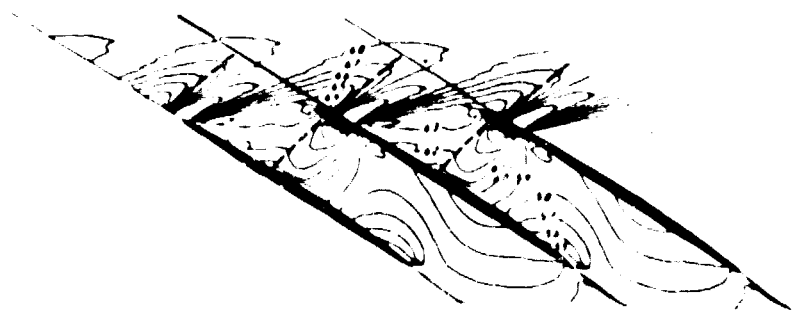

BLADE 3D CALCULATIONS - - - - - SHOCK

Figure 16. - Blade to blade contours of relative flow angle in degrees, 15 percent span from the tip, near stall point. Lightly dashed lines indicate uncertainty in the L.A. contours.

	LA				BLADE3D			
% SPAN FROM TIP	Mrel	β_{rel}	α	ω_s	Mrel	β_{rel}	α	ω_s
15	1.40	62.5	28.0	.061	1.45	62.1	28.	.078

Table 4. Comparison of measured and calculated shock loss parameters, passage shock, mid-gap, near stall point.

The shock structure at 15 percent span from the tip is shown in Figures 15 and 16 which compare computed and measured contours of relative Mach numbers and flow angles. Unlike the tip Mach number contours for the maximum flow case in Figure 8, Figure 15 shows a pronounced bow wave and passage shock system with excellent agreement between the BLADE3D and LA results. Computed relative Mach numbers leaving the shock are low, however. The wake-like contours leaving the trailing edges in the computed results show an inviscid trailing edge slip line. Relative flow angle contours in Figure 16 show an upstream angle of 68 to 69 degrees. The suction surface metal angle at the leading edge is about 64 degrees. The high incidence incoming flow turns smoothly through expansion fans originating one or two blades away to become well aligned with the suction surface at the leading edge.

Table 4 compares the measured and computed shock loss parameters. Since the passage shock is well defined in this case, the shock location and angle are relatively easy to determine. Slight discrepancies in flow conditions ahead of the shock account for a small disagreement in the shock loss parameters.

CONCLUDING REMARKS

Current laser anemometer (LA) measurements are of sufficient accuracy for verification of inviscid codes. Shock smearing in the LA measurements due to seed particle lag is of roughly the same magnitude as numerical shock smearing, and both need to be reduced. Either a better method of estimating boundary layer edge velocities or a means of directly measuring blade surface pressures is needed. More detailed measurements of blade and endwall boundary layers will be needed for verification of viscous codes.

Inviscid calculations from an axisymmetric through-flow code (MERIDL) and a three-dimensional Euler code (BLADE3D) compared well with probe data upstream of the blade row. Downstream, total pressures are high and relative Mach numbers are low due to the neglect of viscous effects. Within the blade row the axisymmetric solutions agree only qualitatively with the other results.

The BLADE3D code accurately predicted Mach number and flow angle distributions and shock structure within an axial compressor rotor at maximum flow and near stall operating points. The near stall solution agrees better with LA measurements than the maximum flow solution does. This is probably because most of the flow turning in the near stall case occurs across a forward passage shock away from viscous effects. But in the maximum flow case a second normal shock near the blade trailing edge (where viscous effects would be greatest) controls the blade row pressure rise. Present results for the maximum flow case have improved on the earlier results given in reference [8]. Bow wave resolution was improved through grid clustering and rear shock structure was improved by adjusting the exit hub static pressure.

Downstream pressure boundary conditions typically needed by Euler codes are difficult to specify. Measured downstream pressures produce erroneous mass flows and shock structures because measured pressures contain viscous losses not accounted for in inviscid codes. Computational times may prohibit iterating on boundary conditions. An axisymmetric through-flow code like MERIDL may be used as a consistent and computationally efficient tool for choosing downstream boundary values. MERIDL input includes upstream total conditions, mass flow, and whirl, and downstream whirl, all input as measured. Shock losses must be specified and may be estimated using the Miller-Hartmann model along with measured probe data. Loss distribution through the blade row does not significantly effect the computed up or downstream solution. Downstream pressures calculated in this manner are higher than measured pressures but are appropriate boundary values for Euler codes, producing the best agreement between mass flows and shock structures measured in a viscous flow and computed inviscidly. In future three-dimensional viscous codes the measured downstream pressure should suffice.

REFERENCES

1. Miller, G. R., Hartmann, M. J., "Experimental Shock Configuration and Shock Losses in a Transonic Compressor Rotor at Design Speed," NACA RM E58A18b, June 5, 1958.
2. Moore, R. D., Lewis, G. W. Jr., Osborn, W. M., "Performance of a Transonic Fan Stage Design for a Low Meridional Velocity Ratio," NASA TP-1298, 1978.
3. Katsanis, T., McNally, W. D., "Revised FORTRAN Program for Calculating Velocities and Streamlines on the Hub-Shroud Midchannel Stream Surface of an Axial-, Radial-, or Mixed-Flow Turbomachine or Annular Duct, I - User's Manual," NASA TN D-8430, March, 1977.
4. Powell, J. A., Strazisar, A. J., Seasholtz, R. G., "Efficient Laser Anemometer for Intra-Rotor Flow Mapping in Turbomachinery," ASME Journal of Engineering for Power, April, 1981, pp. 424 - 429.
5. Strazisar, A. J., Powell, J. A., "Laser Anemometer Measurements In a Transonic Axial Flow Compressor Rotor," ASME Journal of Engineering for Power, April, 1981, pp. 430 - 437.
6. Thompkins, W. T. Jr., "A FORTRAN Program for Calculating Three-Dimensional Inviscid Rotational Flows with Shock Waves in Axial Compressor Rotors," NASA Contractor Report to be published fourth quarter, 1981.
7. Steger, J. L., Pulliam, T. H., Chima, R. V., "An Implicit Finite Difference Code for Inviscid and Viscous Cascade Flow," AIAA Paper no. 80-1427, July, 1980.
8. Strazisar, A. J., Chima, R. V., "Comparison Between Optical Measurements and a Numerical Solution of the Flow Field Within a Transonic Axial-Flow Compressor Rotor," AIAA Paper no. 80-1078, June, 1980.
9. Epstein, A. H., "Quantitative Density Visualization in a Transonic Compressor Rotor," ASME Journal of Engineering for Power, July, 1977, pp. 460 - 474.
10. Schodl, R., "On the Development of a New Optical Method for Flow Measurements in Turbomachines," ASME Paper 74-GT-157, 1974.
11. Schodl, R., "A Laser-Two-Focus (L2F) Velocimeter for Automatic Flow Measurements in the Rotating Components of Turbomachines," in Measurement Methods in Rotating Components of Turbomachinery, ed. by Lakshminarayana, B., and Runstadler, P. Jr., pub. by ASME, N. Y., 1980.
12. Dunker, R. J., Strinning, P. E., Weyer, H. B., "Experimental Study of the Flow Field Within a Transonic Axial Compressor Rotor by Laser Velocimetry and Comparison with Through-Flow Calculations," ASME Journal of Engineering for Power, Vol. 100, no. 2, April, 1978, pp. 279 - 286.
13. Dunker, R. J., Strinning, P. E., "Flow Velocity Measurements Inside of a Transonic Axial Compressor Rotor by Means of an Optical Technique and Compared with Blade-to Blade Calculations," Third International Symposium on Airbreathing Engines, Munich, Germany, March, 1976.
14. Smart, A. E., Wisler, D. C., Mayo, W. T. Jr., "Optical Advances in Laser Transit Anemometry," ASME Journal of Engineering for Power, April, 1981.
15. Wisler, D. C., "Shock Wave and Flow Velocity Measurements in a High Speed Fan Rotor Using the Laser Velocimeter," ASME Paper 76-GT-49, March, 1976.
16. McDonald, P. W., Bolt, C. R., Dunker, R. J., Weyer, H. B., "A Comparison Between Measured and Computed Flow Fields in a Transonic Compressor Rotor," ASME Paper 80-GT-7, 1980.
17. Denton, J. D., Singh, U. K., "Time Marching Methods for Turbomachinery Flow Calculations, Part I: Basic Principles and 2-D Applications, Part II: Three-Dimensional Flows," in Application of Numerical Methods to Flow Calculations in Turbomachines, Von Karman Institute For Fluid Dynamics Lecture Series, April 23 - 27, 1979.
18. Haymann-Haber, G., Thompkins, W. T. Jr., "Comparison of Experimental and Computational Shock Structure in a Transonic Compressor Rotor," ASME Journal of Engineering for Power, Vol. 103, Jan., 1981, pp. 78 - 88.
19. MacCormack, R. W., "Computational Efficiency Achieved by Time Splitting of Finite Difference Operators," AIAA Paper 72-154, 1972.